# Incorporation of graphene into SnO2 photoanodes for dye-sensitized solar cells

# Incorporation of graphene into $SnO_2$ photoanode for dye-sensitized solar cells

Munkhbayar Batmunkh [a,b,1], Mahnaz Dadkhah [b,1], Cameron J. Shearer [b], Mark J. Biggs [a,c], Joseph G. Shapter [b,*]

[a] School of Chemical Engineering, The University of Adelaide, Adelaide, South Australia 5005, Australia

[b] Centre for Nanoscale Science and Technology, School of Chemical and Physical Sciences, Flinders University, Bedford Park, Adelaide, South Australia 5042, Australia

[c] School of Science, Loughborough University, Loughborough, Leicestershire, LE11 3TU, UK

Corresponding author: Joseph G. Shapter,
E-mail: joe.shapter@flinders.edu.au; Tel: (+61) 08 82012005

[1] These authors contributed equally

## Abstract

In dye-sensitized solar cell (DSSC) photoanodes, tin dioxide ($SnO_2$) structures are promising alternative semiconducting oxide to the conventional titania ($TiO_2$), but they suffer from poor photovoltaic (PV) efficiency caused by insufficient dye adsorption and low energy value of the conduction band. A hybrid structure consisting of $SnO_2$ and reduced graphene oxide ($SnO_2$–RGO) was synthesized via a microwave-assisted method and has been employed as a photoanode in DSSCs. Incorporation of RGO into the $SnO_2$ photoanode enhanced the power conversion efficiency of DSSC device by 91.5%, as compared to the device assembled without RGO. This efficiency improvement can be attributed to increased dye loading, enhanced electron transfer and addition of suitable energy levels in of the photoanode. Finally, the use of RGO addresses the major shortcoming of $SnO_2$ when employed as a DSSC photoanode, namely poor dye adsorption and slow electron transfer rate.

## Keywords

Photovoltaic, dye-sensitized solar cells, photoanodes, tin dioxide, graphene

## 1. Introduction

One of the mature developments in new energy production approaches is the dye-sensitized solar cell (DSSC) [1].For a broad perspective of the field, there are several good reviews available [2-4]. A typical DSSC photoanode is made using a transparent conducting oxide (TCO) substrate, wide band gap oxide semiconductor and dye sensitizer. A nanocrystalline $TiO_2$ semiconductor is mostly used as the semiconductor due to its unique properties [5]. Despite the high power conversion efficiencies (PCEs) achieved by devices fabricated with $TiO_2$ photoanodes [6-8], the intrinsic low carrier mobility of $TiO_2$ is a matter of great concern [9, 10]. This issue has led many researchers to probe the development of alternative photoanode materials.

Among many alternative semiconductors, $SnO_2$ has been the subject of numerous investigations [11-13]. This is partially due to the fact that $SnO_2$ has a higher electron mobility than $TiO_2$ [14, 15]. Since the first use of $SnO_2$ in DSSCs, significant developments have been made in the $SnO_2$ photoanodes [11, 13]. These developments include morphology control, doping with various species, surface modification, and hybrid structures with other oxide semiconductors [16-18]. Despite the considerable effort to improve $SnO_2$ based photoanodes, a major challenge for $SnO_2$ based DSSCs is still their low performance caused by poor dye adsorption capability [19]. Additionally, the $SnO_2$ photoanode based DSSCs suffer from a low open circuit voltage ($V_{oc}$) value due to the intrinsically low energy of the conduction band of $SnO_2$ [20]. Therefore, addressing these issues is of great importance for the development of $SnO_2$ based photovoltaic (PV) cells. Moreover, although $SnO_2$ possesses higher electron mobility than $TiO_2$, further improvement in the electron transport in $SnO_2$ photoanode would be of great value to maximize the efficiency.

Due to their excellent conductivity, carbon nanotubes (CNTs) and graphene can act to improve electron transport and reduce the charge recombination which results from sluggish charge transport of semiconducting oxide based photoanodes; thus significantly enhancing the PCE of PV cells [21-26]. Over the past few years, researchers have incorporated graphene derivatives into various $TiO_2$ structures and shown remarkable efficiency enhancement [27-30]. However, until now, there has been no report on the use of graphene structures in $SnO_2$ photoanodes for DSSCs. Moreover, the kinetics of dye adsorption and performance enhancement for carbonaceous photoanodes is still unclear, with some studies suggesting contrary results [21, 28, 29, 31, 32]. Therefore, exploring the effect of graphene or reduced graphene oxide (RGO) in $SnO_2$ photoanode based DSSCs would be valuable.

Herein we report a facile preparation of hybrid structures based on morphologically controllable $SnO_2$ combined with RGO for use as a photoanode in DSSCs. To the best of our knowledge, this work is the first effort involving the application of a graphene structure in $SnO_2$ photoanode based DSSCs. We found that the incorporation of RGO into the $SnO_2$ film not only enhances the electron transfer rate of the photoanode, it also increases the adsorption of dye molecules into the film, thus greatly improving DSSC performance.

## 2. Experimental

### *2.1.Materials*

All chemicals were purchased from Sigma-Aldrich and used without further purification, unless otherwise stated. Tin (II) chloride dihydrate ($SnCl_2 \cdot 2H_2O$) powder (>99% purity, Merck) was used as a starting material. Flourine-doped tin oxide (FTO) coated glass electrode with a sheet resistance ($R_s$) of ~12 Ω/□ (TCO30-8), Ruthenizer 535-bisTBA (N719 dye), iodide/tri-iodide electrolyte (Iodolyte Z-50), DuPont Surlyn® (Meltonix 1170-60) and Platinum catalyst (Platisol T) were obtained from Solaronix, Switzerland.

### *2.2.Preparation of graphene oxide*

Graphite oxide was prepared from natural graphite using the approach from Marcano et al. [33]. Briefly, a 9:1 (v:v) mixture of sulfuric acid (95-98% $H_2SO_4$) and phosphoric acid (85% $H_3PO_4$) (240:27 mL) was kept in the cold room (3-5$^oC$) until it was added to a mixture of graphite flakes (2 g) and potassium permanganate (99% $KMnO_4$) (12 g). The oxidation process of graphite was carried out by stirring the mixture at ~50$^oC$ for 12 h. Upon completion, the reaction was cooled down to room temperature and poured onto ice (approximately 300 mL) with 30% hydrogen peroxide ($H_2O_2$) (2 mL). The mixture was then washed with distilled (DI) water, 30% hydrochloric acid (HCl) and ethanol (x 2 times). For each sequential wash, the product was centrifuged at 4400 rpm for 3 h and the supernatant decanted away. The obtained light brown sample was then vacuum-dried overnight at room temperature. Then the as-prepared graphite oxide was exfoliated in water (1 mg $mL^{-1}$) by bath ultrasonication (Elma, Germany) for 60 min to obtain homogenous graphene oxide (GO) dispersion.

### *2.3.Synthesis of $SnO_2$-RGO hybrid*

The $SnO_2$-RGO hybrid was prepared using a facile microwave-assisted method [34]. In a typical process, six glass beakers containing 90 mL DI water and different GO content (0 mg,

2 mg, 4.5 mg, 7 mg, 12 mg and 50 mg) were ultrasonicated for 2h. Meanwhile, 1.5 g of $SnCl_2 \cdot 2H_2O$ powder was added into 200 mL of 0.02M HCl solution. Then the previously prepared GO dispersions were added into the $SnCl_2 \cdot 2H_2O$ solutions, followed by stirring for 30 min. The as-obtained mixtures were then reacted using a microwave technique (StartSYNTH Microwave Synthesis Labstation, Milestone s.r.l) for 5 min under 600 W power. The temperature was adjusted to 90$^oC$ during the microwave treatment. After cooling to room temperature, the obtained precipitates were centrifuged at 2000 rpm for 10 min and washed several times with DI water, followed by drying overnight at 80$^oC$ in an oven to obtain $SnO_2$-RGO powders. Finally, six samples of different RGO content (0 wt%, 0.2 wt%, 0.45 wt%, 0.7 wt%, 1.2 wt% and 4.75 wt% in the hybrid) were prepared and have been used for DSSC fabrication. It should be noted that the amount of $SnO_2$ in these samples was not changed. For the calculation of the RGO concentration in the hybrid, it was assumed that the conversion of $SnCl_2 \cdot 2H_2O$ to $SnO_2$ is 100% based on the lack of Cl peak observed in various hybrid characterizations.

### *2.4.Device fabrication*

Firstly, viscous $SnO_2$ and $SnO_2$-RGO pastes were prepared from the previously prepared six samples according to the established procedures described in the literature [35]. FTO coated glass substrates were cleaned by a detergent (Pyroneg), followed by washing with Milli-Q water, acetone and ethanol under ultrasonication for 10 min each and subsequently dried with a nitrogen gas. The cleaned FTO glass subtrates were immersed in a 40 mM $TiCl_4$ aqueous solution at 70$^oC$ for 30 min. Then the $TiCl_4$ treated FTO electrodes were coated with the $SnO_2$ and $SnO_2$-RGO pastes by a doctor blade technique to prepare the photoanodes. All photoanode films were obtained by applying two layers of adhesive scotch tape (*Magic™ Tape, 3M*) on the FTO electrode, which gives a film thickness of ~15 µm [36]. It is well established that the photoanode thickness of 12-16 µm is the optimum condition for achieving high DSSC performance [36-38]. After the deposition of $SnO_2$ and $SnO_2$-RGO pastes onto the FTO substrates, the photoanode films were gradually heated under an air flow at 125$^oC$ for 5 min, 325$^oC$ for 5 min, at 375$^oC$ for 15 min and at 450$^oC$ for 30 min, followed by cooling to room temperature. Then the films were again soaked in 40 mM $TiCl_4$ solution at 70$^oC$ for 30 min, followed by sintering at 450$^oC$ for 30 min. After cooling to ~50$^oC$, the prepared films were immersed into 0.5 mM N719 dye in an ethanol solution for 20 h at 40$^oC$. Then, the dye adsorbed photoanodes were washed with ethanol to remove non-adsorbed dye from the films.

In the meantime, platinum (Pt) catalyst was coated onto FTO substrates from Pt precursor (Solaronix) by a brush-painting method to prepare the counter electrodes. The dye-adsorbed photoanodes and Pt counter electrodes were assembled into a sealed sandwich-type cell, with a 60 μm thick hot-melt sealing Surlyn between each layer. The electrolyte solution, Iodolyte Z-50 (Solaronix), was introduced into the cell via a vacuum-filling method through an injection hole on the counter electrode side. Finally, the hole was sealed with scotch tape.

*2.5.Characterization*

Scanning electron microscopy (SEM) images were obtained using an Inspect F50 SEM (FEI) with accelerating voltage of 10 kV. Energy dispersive X-ray spectroscopy (EDX) analysis was completed on the same system with Team EDS Octane Pro (EDAX) attachment. Elemental compositions of the samples were analyzed at binding energy ranging from 0 eV to 1200 eV using a X-ray photoelectron spectroscopy (XPS), Leybold Heraeus LHS-10 with a SPECS XR-50 dual anode source operating at 250W. The Mg-Kα source, which has energy of 1253.6 eV, was used for the XPS analysis. X-ray diffraction (XRD) patterns were carried out on a powder X-ray diffractometer at 40 kV and 15 mA in the range of $2\theta$ = 3–80° using Cu Kα radiation (Model Miniflex 600, Rigaku, Japan). Attenuated Total Reflection-Fourier Transform Infrared Spectroscopy (ATR-FTIR) spectra were acquired over a wavenumber range of 4000-500 $cm^{-1}$ in transmission mode using a Frontier FTIR spectrometer (Perkin Elmer, USA) with a germanium crystal. Raman spectroscopy was carried out on LabRAM HR Evolution spectrometer (Horiba Jobin Yvon, Japan). Raman spectra were collected using a 532 nm laser (mpc 3000) as the excitation source. A 50x objective was used with a confocal hole size of 100 μm. Auger spectromicroscopy "PHI 710 scanning auger nanoprobe" operating at base vacuum below $1x10^{-9}$ Torr was used to analyse the elemental analysis of the samples. Sputtering samples for the analysis was performed using ultra high purity Argon. Data was collected using an electron beam of 10 kV, 10nA.

To determine the adsorbed amount of dye molecules in the $SnO_2$ and $SnO_2$-RGO films, the dye in the films was dissolved in 0.1 M NaOH aqueous solution and then measured by a Varian Cary 50G UV-vis Spectrophotometer at wavelengths ranging from 300 to 1000 nm. Sheet resistivities were performed on the microscope slide substrate coated with $SnO_2$-only and/or $SnO_2$-RGO hybrid using a four point probe technique (KeithLink Technology Co., Ltd. Taiwan). The photocurrent–voltage (*J*–*V*) characteristics were investigated using a Keithley 2400 SMU instrument and recorded using a custom LabView Virtual Instrument program. A standard silicon test cell with NIST-traceable certification was used to calibrate

the power density as 100 mW $cm^{-2}$ at the sample plane of the collimated xenon-arc light source, which was passed through an AM 1.5G filter. The active area of each device was 0.25 $cm^2$. The *J-V* curves were measured in the air through reverse-scan direction from 1 V to -1 V. Incident-photon-to-current conversion efficiency (IPCE) measurements as a function of wavelength ranging from 400 nm to 800 nm were taken by passing chopped light from a Xenon source through a monochromator and onto the devices.

## 3. Results and discussion

The preparation of $SnO_2$–RGO hybrid is shown in Scheme 1. Firstly, $SnCl_2 \cdot 2H_2O$ powder (Fig. S1) was mixed with GO (Fig. 1a) in aqueous hydrochloric acid (HCl, 0.02 M) to form a homogenous solution, which was stirred and reacted using a microwave technique. During this process, GO was reduced and is termed "RGO". Then, the resulting product was centrifuged and dried to obtain a $SnO_2$-RGO hybrid. For comparison, the same process was carried out in the absence of GO to produce only $SnO_2$ [36].

The SEM image in Fig. 1b shows that the synthesized $SnO_2$ is a 1 dimensional (1D) microstructure with a rod-like shape. It is worth noting that 1D structures can provide fast electron transport pathway [39]. Fig. 1c depicts the SEM image of the $SnO_2$-RGO hybrid, which demonstrates clear differences compared to GO (Fig. 1a) and $SnO_2$-only. It can be seen that the $SnO_2$ micro-rods were well mixed and wrapped in the RGO flakes, as expected, to form the hybrid material. As shown in Fig. 1d and 1e, during the microwave-assisted synthesis, small $SnO_2$ nanoparticles were also formed on both $SnO_2$ rods and RGO flakes which are expected to be beneficial for dye adsorption.

Fig. 2a shows the XRD patterns of GO, $SnO_2$-only and $SnO_2$-RGO hybrid. GO displays an intense peak at around $2\theta$ = 10.9°, which corresponds to the (002) reflection of the stacked GO nanosheets [40]. It can be observed that the $SnO_2$-only sample shows broad and weak peaks ((110), (101), (200), (211) and (112)), which can be indexed to a tetragonal-structured $SnO_2$ with poor crystallinity [41]. It is well known that after the reduction process, the diffraction peak of the GO shifts to around $2\theta$ = 24.5°. This peak at $2\theta$ = 24.5° cannot be observed in the XRD pattern of the hybrid because this peak will be overlapped with the $SnO_2$ peak (110). Another noticeable feature in the XRD pattern of $SnO_2$-RGO is that the $SnO_2$ in the hybrid shows narrow and strong peaks, which can be assigned to a tetragonal structure (JCPDS card no. 41-1445), indicating an improved crystallinity of $SnO_2$ and larger

average crystal size [42]. This improvement in the crystallinity is often observed in nanocarbon-metal oxide materials and is attributed to a heat-sink effect in which the nanocarbon facilitates crystallization via heat transfer [43].

The results of the XRD analysis were further confirmed by characterizing the samples using XPS (Fig. 2b), ATR-FTIR (Fig. 3a) and Raman spectroscopy (Fig. 3b). It can be clearly observed from the Raman spectra of the $SnO_2$-RGO hybrid (Fig. 3b) that the $I_D/I_G$ ratio of RGO increased compared to that of the GO. This increase in the $I_D/I_G$ ratio can be attributed to the defects caused during reduction of GO [27]. Moreover, it should be noted that in the XPS survey spectra, negligible peaks (Cl 2p) can be found in the $SnO_2$-based samples, which could be attributed to the unreacted $Cl^-$ of $SnCl_2{\cdot}2H_2O$. Additionally, Auger and EDX elemental analysis were carried out on selected area of SEM images of the $SnO_2$-RGO hybrid and reveal small amount of chlorine remaining in the sample (see Fig. S2). These results of Auger and EDX spectroscopies were in good agreement with the XPS and may explain the sample crystallinity.

To study the influence of RGO on the efficiency of PV cells, DSSCs were fabricated using six photoanodes of different RGO content in the hybrid and were evaluated using simulated AM1.5 sunlight with an output power of 100 mW $cm^{-2}$. Notably, for the fabrication of DSSCs, the photoanodes were immersed in a $TiCl_4$ aqueous solution before they were soaked in the dye solution. This process is a commonly followed strategy to deposit a thin layer of $TiO_2$ over $SnO_2$ ($SnO_2$-RGO in our case) which can improve the $V_{oc}$ of the $SnO_2$-based DSSCs [18, 44-46]. Therefore, the photoanodes were denoted as "$TiO_2$-$SnO_2$-RGO (X)", where the value of X indicates the weight concentration (wt%) of RGO in the hybrid. For example, the photoanode film prepared with 0.2 wt% RGO is denoted "$TiO_2$-$SnO_2$-RGO (0.2)".

The photocurrent density–voltage (*J–V*) characteristics of the DSSCs assembled with these photoanodes are shown in Fig. 4a and the corresponding PV parameters have been summarized in Table 1. The control DSSC device ($TiO_2$-$SnO_2$-RGO (0)) fabricated based on $SnO_2$ photoanode without RGO showed an average PCE ($\eta$) of 1.28 ± 0.52% with a short–circuit current ($J_{sc}$) value of 4.78 ± 0.95 mA $cm^{-2}$ and $V_{oc}$ of 0.64 ± 0.01V which are typical values for such cells [12, 18].

It can be seen from Table 1 that from $TiO_2$-$SnO_2$-RGO (0) to $TiO_2$-$SnO_2$-RGO (0.7) (increasing RGO content), the $J_{sc}$ value increases from 4.78 ± 0.95 to 10.23 ± 0.88 mA $cm^{-2}$. We hypothesize that this increase in the $J_{sc}$ is due to the improved dye loading into the film and enhanced electron transfer within the photoanode [22, 27, 28]. In order to confirm our hypothesis, we fabricated $SnO_2$ films (Fig. S3) with different RGO content and investigated the dye adsorption capability of the films. No treatment with $TiCl_4$ solution was done to allow the effect of RGO in the $SnO_2$ film on the extent of dye adsorption to be probed without any interference. As shown in Fig. S3, the films after dye adsorption and also the solutions after subsequent desorption of the dye molecules using NaOH show that the dye adsorption of the $SnO_2$ films was significantly improved by incorporating RGO. Moreover, UV-vis spectra in Fig. 4b show the absorbance of dye desorbed from the films and shows that dye adsorption increases with increasing RGO concentration in the hybrid. This improvement in the dye adsorption is most likely due to a better matching of the molecular nature of the N719 dye and the chemical nature of the hybrid. N719 has both polar groups and aromatic regions. Since our RGO was derived from GO, some functional groups (–OH, –COOH etc.) would remain on the surface of RGO due to the partial reduction and these would interact with the polar groups on N719. These functional groups may be playing an important role in the dye adsorption [21]. $SnO_2$ would also interact with these polar groups. The introduction of the RGO provides some aromatic nature to the hybrid and one can speculate that this will create polar and aromatic regions in close proximity and will further enhance dye adsorption. Additionally the high-surface area of RGO may contribute to the adsorption of the dye [28]. Interestingly, the dye adsorption of the film with the highest RGO content (4.75 wt%) is starting to saturate, indicating that adding more RGO into the film would likely not lead to significant further increases in dye adsorption (see Fig. S4).

To determine the mechanism for the improved $J_{sc}$ value, the resistivity ($R_s$) of the $TiCl_4$ treated $SnO_2$ film without and with 0.45 wt% RGO was measured using a four point probe. The same film thickness on a glass substrate was obtained using the doctor blade method (see experimental details). The film without RGO shows a $R_s$ of 4.51 x $10^6$ Ω/□, while the RGO incorporated film exhibits a comparatively low $R_s$ (1.81 x $10^6$ Ω/□) (see Table S1). The decrease in the $R_s$ (nearly 3-fold) of the film with RGO is due to the fact that high conductivity of the RGO in the hybrid reduces the interfacial resistance between $SnO_2$. In addition, the measured series resistance ($R_{series}$) of the $TiO_2$-$SnO_2$-RGO (0.45) based DSSC was 97.9 Ω, which was ~1.7-fold lower than that of the control cell (Table S1). On the basis

of these results, it is clear that the presence of RGO accelerated electron transport process within the photoanode and suppressed the charge recombination of the cells; thus significantly enhancing the $\eta$ [21, 22, 28].

However, although $TiO_2$-$SnO_2$-RGO (0.7) based cell showed the highest $J_{sc}$ (10.95 mA $cm^{-2}$), the measured average $\eta$ (2.08 ± 0.17%) was not the best observed, despite the films having high dye adsorption. When the RGO concentration in the hybrid further increased to 1.2 wt% and 4.75 wt%, a significant drop in the $J_{sc}$ value and $V_{oc}$ was observed for the $TiO_2$-$SnO_2$-RGO (1.2) and $TiO_2$-$SnO_2$-RGO (4.75) based DSSCs, thus resulting in very poor efficiencies. We attribute this $\eta$ decrease of the DSSCs with higher RGO loading to (i) opacity of the film (see films before dye adsorption in Fig. S3) reducing light absorption and (ii) high catalytic property of RGO, which has been shown to limit the continuous electron transfer at the photoanode [2, 21, 47].

It is well established that although carbon materials can facilitate electron transport in the DSSC, the catalytic activity of carbon materials toward reduction of the electrolyte causes significant charge recombination at the interface of the photoanode and electrolyte (since this reaction should only occur at the cathode) if too high concentration of carbon is used [2]. Fig. 4c shows the dark *J*–*V* characteristics of DSSCs fabricated without and with RGO in the $SnO_2$ photoanodes. It is known that the magnitude and onset of the dark current indicates the level of charge recombination between the electrons from the dye excitation process and the $I_3^-$ ions in the electrolyte [48]. It can be seen that the dark current onset shifted to a lower potential after adding a small amount of RGO into the $SnO_2$ photoanodes. This is known to be due to the increased charge recombination rate of the DSSCs caused by the reaction between the RGO and electrolyte. Therefore, at a given voltage, the dark current increased when the RGO was added into the $SnO_2$ photoanode of DSSC. Our finding is in line with similar report of adding carbon powders into $TiO_2$ photoanodes [48].

Indeed, the highest $\eta$ (3.16%) with an average $\eta$ of 2.94 ± 0.24% was achieved for the device based on $TiO_2$-$SnO_2$-RGO (0.45). In the $TiO_2$-$SnO_2$-RGO based DSSC, the $TiO_2$ can act as a barrier layer reducing the contact of RGO with the electrolyte and therefore reducing the likelihood of RGO catalyzing recombination at the photoanode. Taking into account the $TiO_2$ deposition process (dip coating) which unlikely to achieve 100 % coverage, we speculate that with higher RGO content the net amount of RGO in contact with the electrolyte will increase

accordingly. Moreover, we fabricated $SnO_2$ and $SnO_2$-RGO photoanodes based DSSCs without $TiCl_4$ treatment and their PV results have been plotted in Fig. S5a. The efficiencies of these DSSCs were ~2-fold lower than those of the devices fabricated with $TiCl_4$ treatment, confirming that the use of $TiCl_4$ treatment is a vital method to enhance the cell performance in $SnO_2$ photoanode DSSCs.

It can be seen from Table 1 that all parameters of DSSC fabricated with $SnO_2$ photoanodes increased after incorporating 0.45 wt% RGO. The calculated $\eta$ enhancement of $TiO_2$-$SnO_2$-RGO (0.45) photoanode based device was impressive (91.5%) as compared to the control cell especially in light of the fact that a very small amount of RGO is required to realise these large improvements in efficiency. This photoanode ($TiO_2$-$SnO_2$-RGO (0.45)) was chosen for further investigation to fully understand the role of RGO in the DSSC.

IPCE spectra offer important information on the light harvesting efficiency which is mainly determined by the absorption of light by the dye molecules at the photoanode and electron transport processes. The IPCE spectra of the DSSCs with and without RGO in the photoanode are illustrated in Fig. 4d. It should be noted that the IPCE spectra of the DSSCs were characterized after the devices were aged for approximately 10 days. The IPCE of the $TiO_2$-$SnO_2$-RGO (0.45) photoanode based device is higher than that of the control DSSC over the entire wavelength region. The lack of wavelength dependence indicates that the addition of RGO into the $SnO_2$ photoanode improves the DSSC performance without altering the internal mechanism, likely by enhancing electron transfer rate and increasing dye adsorption onto the photoanode.

As discussed earlier, RGO in the hybrid ensures rapid electron transport process (Fig. 5a) and significantly enhances the $J_{sc}$ value of the DSSC. Importantly, it can be expected that incorporation of RGO in the $SnO_2$ photoanode would improve the DSSC performance owing to presence of suitable energy levels. Fig. 5b shows an energy level diagram for the $TiCl_4$ treated $SnO_2$ photoanode with RGO. Since a thin $TiO_2$ layer was deposited on the FTO and on the $SnO_2$ or $SnO_2$-RGO layers by $TiCl_4$ treatment, it is reasonable to include the energy level of $TiO_2$ in this diagram. The red arrow in Fig. 5b represents the fact that the electron transfer from the conduction band of $SnO_2$ to that of $TiO_2$ is not possible due to their mismatching band energy levels. As the $TiO_2$ coverage on the FTO is incomplete (not 100%), both $SnO_2$ and $TiO_2$ are in contact with the FTO and hence electron transfer from both the

$SnO_2$ and $TiO_2$ to the FTO is still feasible. The results from Fig. S6 and S7 show that despite the fact that the $TiO_2$ on the FTO is very thin, it does make a contribution to the current and voltage of the cell and as such is important to show. Since the energy level of RGO (-4.40 eV) lies between the conduction band of $TiO_2$ (-4.26 eV) and $SnO_2$ (-4.56 eV), the electrons can be rapidly transferred stepwise from the $TiO_2$ to the $SnO_2$ conduction band (see Fig. 5b) [18, 28].Here RGO can act as a bridge between $TiO_2$ and $SnO_2$. This effective electron transfer would likely reduce the charge recombination of the cell, thus improves the performance.

Finally, the PV parameters of our best-performing cells have been compared with values reported in the literature for other DSSCs with $SnO_2$ based photoanodes. Table 2 summarizes the PV parameters such as $J_{sc}$, $V_{oc}$, *FF* and $\eta$ of DSSC devices fabricated with various $SnO_2$ structures based photoanodes and our best performing cells. It can be observed from Table 2 that the efficiency observed for our DSSC fabricated with $SnO_2$-RGO photoanode is comparable or higher than those achieved by other 1D and 3D $SnO_2$ structured photoanode films. Therefore, this indicates that the incorporation of graphene structures into $SnO_2$ photoanode is an effective strategy to achieve high efficiency DSSCs.

## 4. Conclusion

In summary, the successful application of RGO structures in 1D $SnO_2$ micro-rod based photoanodes for DSSCs has been demonstrated. Herein we show that the application of RGO overcomes the major shortcoming of $SnO_2$ when applied as a DSSC photoanode, namely poor dye adsorption. In addition, owing to its suitable energy levels and excellent conductivity, RGO significantly improved the electron transport rate in the cells. Importantly, PCE ($\eta$) of the DSSC was significantly improved to 3.16% by incorporating a very small amount of RGO into the photoanode, demonstrating a ~91.5% enhancement in the efficiency when compared to $SnO_2$-only photoanode based DSSC (1.65%).

**Acknowledgements**

The support of the Australian Research Council Discovery Program (DP130101714) is gratefully acknowledged. Munkhbayar Batmunkh acknowledges International Postgraduate Research Scholarship (IPRS) and Australian Postgraduate Award (APA) for their financial support during his study in Australia. We acknowledge the use of

South Australian node of the Australian Microscopy & Microanalysis Research Facility (AMMRF) at Flinders University.

## Appendix A. Supplementary data

Supplementary data associated with this article can be found, in the online version.

## References

[1] G. Hashmi, K. Miettunen, T. Peltola, J. Halme, I. Asghar, K. Aitola, M. Toivola, P. Lund, Review of materials and manufacturing options for large area flexible dye solar cells, Renewable and Sustainable Energy Reviews, 15 (2011) 3717-3732.
[2] M. Batmunkh, M.J. Biggs, J.G. Shapter, Carbon Nanotubes for Dye-Sensitized Solar Cells, Small, 11 (2015) 2963-2989.
[3] F. Bella, C. Gerbaldi, C. Barolo, M. Gratzel, Aqueous dye-sensitized solar cells, Chemical Society Reviews, 44 (2015) 3431-3473.
[4] J. Wu, Z. Lan, J. Lin, M. Huang, Y. Huang, L. Fan, G. Luo, Electrolytes in Dye-Sensitized Solar Cells, Chemical Reviews, 115 (2015) 2136-2173.
[5] Y. Hao, E. Gabrielsson, P.W. Lohse, W. Yang, E.M.J. Johansson, A. Hagfeldt, L. Sun, G. Boschloo, Peripheral Hole Acceptor Moieties on an Organic Dye Improve Dye-Sensitized Solar Cell Performance, Advanced Science, 2 (2015) 1500174.
[6] L. Han, A. Islam, H. Chen, C. Malapaka, B. Chiranjeevi, S. Zhang, X. Yang, M. Yanagida, High-efficiency dye-sensitized solar cell with a novel co-adsorbent, Energy & Environmental Science, 5 (2012) 6057-6060.
[7] S. Mathew, A. Yella, P. Gao, R. Humphry-Baker, F.E. CurchodBasile, N. Ashari-Astani, I. Tavernelli, U. Rothlisberger, K. NazeeruddinMd, M. Grätzel, Dye-sensitized solar cells with 13% efficiency achieved through the molecular engineering of porphyrin sensitizers, Nat Chem, 6 (2014) 242-247.
[8] S.G. Hashmi, M. Ozkan, J. Halme, K.D. Misic, S.M. Zakeeruddin, J. Paltakari, M. Grätzel, P.D. Lund, High performance dye-sensitized solar cells with inkjet printed ionic liquid electrolyte, Nano Energy, 17 (2015) 206-215.
[9] A.K. Chandiran, M. Abdi-Jalebi, M.K. Nazeeruddin, M. Grätzel, Analysis of Electron Transfer Properties of ZnO and TiO2 Photoanodes for Dye-Sensitized Solar Cells, ACS Nano, 8 (2014) 2261-2268.
[10] J. Fan, Z. Li, W. Zhou, Y. Miao, Y. Zhang, J. Hu, G. Shao, Dye-sensitized solar cells based on TiO2 nanoparticles/nanobelts double-layered film with improved photovoltaic performance, Applied Surface Science, 319 (2014) 75-82.
[11] S. Ferrere, A. Zaban, B.A. Gregg, Dye Sensitization of Nanocrystalline Tin Oxide by Perylene Derivatives, The Journal of Physical Chemistry B, 101 (1997) 4490-4493.
[12] Q. Wali, A. Fakharuddin, I. Ahmed, M.H. Ab Rahim, J. Ismail, R. Jose, Multiporous nanofibers of SnO2 by electrospinning for high efficiency dye-sensitized solar cells, Journal of Materials Chemistry A, 2 (2014) 17427-17434.
[13] Q. Wali, A. Fakharuddin, R. Jose, Tin oxide as a photoanode for dye-sensitised solar cells: Current progress and future challenges, Journal of Power Sources, 293 (2015) 1039-1052.
[14] I. Concina, A. Vomiero, Metal Oxide Semiconductors for Dye- and Quantum-Dot-Sensitized Solar Cells, Small, 11 (2015) 1744-1774.
[15] E. Ramasamy, J. Lee, Ordered Mesoporous SnO2−Based Photoanodes for High-Performance Dye-Sensitized Solar Cells, The Journal of Physical Chemistry C, 114 (2010) 22032-22037.
[16] S. Gubbala, V. Chakrapani, V. Kumar, M.K. Sunkara, Band-Edge Engineered Hybrid Structures for Dye-Sensitized Solar Cells Based on SnO2 Nanowires, Advanced Functional Materials, 18 (2008) 2411-2418.

[17] J. Gong, H. Qiao, S. Sigdel, H. Elbohy, N. Adhikari, Z. Zhou, K. Sumathy, Q. Wei, Q. Qiao, Characteristics of SnO2 nanofiber/TiO2 nanoparticle composite for dye-sensitized solar cells, AIP Advances, 5 (2015) 067134.
[18] A. Thapa, J. Zai, H. Elbohy, P. Poudel, N. Adhikari, X. Qian, Q. Qiao, TiO2 coated urchin-like SnO2 microspheres for efficient dye-sensitized solar cells, Nano Research, 7 (2014) 1154-1163.
[19] C.-L. Wang, J.-Y. Liao, Y. Zhao, A. Manthiram, Template-free TiO2 hollow submicrospheres embedded with SnO2 nanobeans as a versatile scattering layer for dye-sensitized solar cells, Chemical Communications, 51 (2015) 2848-2850.
[20] A. Birkel, Y.-G. Lee, D. Koll, X.V. Meerbeek, S. Frank, M.J. Choi, Y.S. Kang, K. Char, W. Tremel, Highly efficient and stable dye-sensitized solar cells based on SnO2 nanocrystals prepared by microwave-assisted synthesis, Energy & Environmental Science, 5 (2012) 5392-5400.
[21] M. Batmunkh, M.J. Biggs, J.G. Shapter, Carbonaceous Dye-Sensitized Solar Cell Photoelectrodes, Advanced Science, 2 (2015) 1400025.
[22] J.D. Roy-Mayhew, I.A. Aksay, Graphene Materials and Their Use in Dye-Sensitized Solar Cells, Chemical Reviews, 114 (2014) 6323-6348.
[23] M. Batmunkh, C.J. Shearer, M.J. Biggs, J.G. Shapter, Nanocarbons for mesoscopic perovskite solar cells, Journal of Materials Chemistry A, 3 (2015) 9020-9031.
[24] A. Kongkanand, R. Martínez Domínguez, P.V. Kamat, Single Wall Carbon Nanotube Scaffolds for Photoelectrochemical Solar Cells. Capture and Transport of Photogenerated Electrons, Nano Letters, 7 (2007) 676-680.
[25] S.-B. Kim, J.-Y. Park, C.-S. Kim, K. Okuyama, S.-E. Lee, H.-D. Jang, T.-O. Kim, Effects of Graphene in Dye-Sensitized Solar Cells Based on Nitrogen-Doped TiO2 Composite, The Journal of Physical Chemistry C, 119 (2015) 16552-16559.
[26] A. Sacco, S. Porro, A. Lamberti, M. Gerosa, M. Castellino, A. Chiodoni, S. Bianco, Investigation of Transport and Recombination Properties in Graphene/Titanium Dioxide Nanocomposite for Dye-Sensitized Solar Cell Photoanodes, Electrochimica Acta, 131 (2014) 154-159.
[27] Z. He, G. Guai, J. Liu, C. Guo, J.S. Chye Loo, C.M. Li, T.T.Y. Tan, Nanostructure control of graphene-composited TiO2 by a one-step solvothermal approach for high performance dye-sensitized solar cells, Nanoscale, 3 (2011) 4613-4616.
[28] Y.-B. Tang, C.-S. Lee, J. Xu, Z.-T. Liu, Z.-H. Chen, Z. He, Y.-L. Cao, G. Yuan, H. Song, L. Chen, L. Luo, H.-M. Cheng, W.-J. Zhang, I. Bello, S.-T. Lee, Incorporation of Graphenes in Nanostructured TiO2 Films via Molecular Grafting for Dye-Sensitized Solar Cell Application, ACS Nano, 4 (2010) 3482-3488.
[29] T. Chen, W. Hu, J. Song, G.H. Guai, C.M. Li, Interface Functionalization of Photoelectrodes with Graphene for High Performance Dye-Sensitized Solar Cells, Advanced Functional Materials, 22 (2012) 5245-5250.
[30] Y.H. Ng, I.V. Lightcap, K. Goodwin, M. Matsumura, P.V. Kamat, To What Extent Do Graphene Scaffolds Improve the Photovoltaic and Photocatalytic Response of TiO2 Nanostructured Films?, The Journal of Physical Chemistry Letters, 1 (2010) 2222-2227.
[31] P. Brown, K. Takechi, P.V. Kamat, Single-Walled Carbon Nanotube Scaffolds for Dye-Sensitized Solar Cells, The Journal of Physical Chemistry C, 112 (2008) 4776-4782.
[32] K.T. Dembele, G.S. Selopal, C. Soldano, R. Nechache, J.C. Rimada, I. Concina, G. Sberveglieri, F. Rosei, A. Vomiero, Hybrid Carbon Nanotubes–TiO2 Photoanodes for High Efficiency Dye-Sensitized Solar Cells, The Journal of Physical Chemistry C, 117 (2013) 14510-14517.
[33] D.C. Marcano, D.V. Kosynkin, J.M. Berlin, A. Sinitskii, Z. Sun, A. Slesarev, L.B. Alemany, W. Lu, J.M. Tour, Improved Synthesis of Graphene Oxide, ACS Nano, 4 (2010) 4806-4814.
[34] L. Yin, D. Chen, X. Cui, L. Ge, J. Yang, L. Yu, B. Zhang, R. Zhang, G. Shao, Normal-pressure microwave rapid synthesis of hierarchical SnO2@rGO nanostructures with superhigh surface areas as high-quality gas-sensing and electrochemical active materials, Nanoscale, 6 (2014) 13690-13700.
[35] Y. Xiong, D. He, Y. Jin, P.J. Cameron, K.J. Edler, Ordered Mesoporous Particles in Titania Films with Hierarchical Structure as Scattering Layers in Dye-Sensitized Solar Cells, The Journal of Physical Chemistry C, 119 (2015) 22552-22559.

[36] M. Batmunkh, M. Dadkhah, C.J. Shearer, M.J. Biggs, J.G. Shapter, Tin oxide light scattering layer for titania photoanodes in dye-sensitized solar cells, Energy Technology, 4 (2016) DOI: 10.1002/ente.201600008.
[37] L. Yang, W.W.-F. Leung, Electrospun TiO2 Nanorods with Carbon Nanotubes for Efficient Electron Collection in Dye-Sensitized Solar Cells, Advanced Materials, 25 (2013) 1792-1795.
[38] S. Ito, T.N. Murakami, P. Comte, P. Liska, C. Grätzel, M.K. Nazeeruddin, M. Grätzel, Fabrication of thin film dye sensitized solar cells with solar to electric power conversion efficiency over 10%, Thin Solid Films, 516 (2008) 4613-4619.
[39] P. Poudel, Q. Qiao, One dimensional nanostructure/nanoparticle composites as photoanodes for dye-sensitized solar cells, Nanoscale, 4 (2012) 2826-2838.
[40] Y.-T. Xu, Y. Guo, H. Jiang, X.-B. Xie, B. Zhao, P.-L. Zhu, X.-Z. Fu, R. Sun, C.-P. Wong, Enhanced Performance of Lithium-Ion Batteries with Copper Oxide Microspheres @ Graphene Oxide Micro/Nanocomposite Electrodes, Energy Technology, 3 (2015) 488-495.
[41] M. Dadkhah, M. Salavati-Niasari, Controlled synthesis of tin dioxide nanostructures via two simple methods and the influence on dye sensitized solar cell, Electrochimica Acta, 129 (2014) 62-68.
[42] A.L. Patterson, The Scherrer Formula for X-Ray Particle Size Determination, Physical Review, 56 (1939) 978-982.
[43] Z. Ren, E. Kim, S.W. Pattinson, K.S. Subrahmanyam, C.N.R. Rao, A.K. Cheetham, D. Eder, Hybridizing photoactive zeolites with graphene: a powerful strategy towards superior photocatalytic properties, Chemical Science, 3 (2012) 209-216.
[44] J. Qian, P. Liu, Y. Xiao, Y. Jiang, Y. Cao, X. Ai, H. Yang, TiO2-Coated Multilayered SnO2 Hollow Microspheres for Dye-Sensitized Solar Cells, Advanced Materials, 21 (2009) 3663-3667.
[45] M.-S. Wu, Z.-Z. Ceng, C.-Y. Chen, Surface modification of porous TiO2 electrode through pulse oxidative hydrolysis of TiCl3 as an efficient light harvesting photoanode for dye-sensitized solar cells, Electrochimica Acta, 191 (2016) 256-262.
[46] Q. Yi, S. Cong, H. Wang, Y. Wang, X. Dai, J. Zhao, Y. Sun, Y. Lou, G. Zou, High-stability Ti4+ precursor for the TiO2 compact layer of dye-sensitized solar cells, Applied Surface Science, 356 (2015) 587-592.
[47] J. Chen, B. Li, J. Zheng, J. Zhao, Z. Zhu, Role of Carbon Nanotubes in Dye-Sensitized TiO2-Based Solar Cells, The Journal of Physical Chemistry C, 116 (2012) 14848-14856.
[48] S.H. Kang, J.-Y. Kim, Y.-K. Kim, Y.-E. Sung, Effects of the incorporation of carbon powder into nanostructured TiO2 film for dye-sensitized solar cell, Journal of Photochemistry and Photobiology A: Chemistry, 186 (2007) 234-241.
[49] M.-H. Kim, Y.-U. Kwon, Semiconducting Divalent Metal Oxides as Blocking Layer Material for SnO2-Based Dye-Sensitized Solar Cells, The Journal of Physical Chemistry C, 115 (2011) 23120-23125.
[50] Y. Duan, J. Zheng, N. Fu, Y. Fang, T. Liu, Q. Zhang, X. Zhou, Y. Lin, F. Pan, Enhancing the performance of dye-sensitized solar cells: doping SnO2 photoanodes with Al to simultaneously improve conduction band and electron lifetime, Journal of Materials Chemistry A, 3 (2015) 3066-3073.
[51] C. Gao, X. Li, X. Zhu, L. Chen, Z. Zhang, Y. Wang, Z. Zhang, H. Duan, E. Xie, Branched hierarchical photoanode of titanium dioxide nanoneedles on tin dioxide nanofiber network for high performance dye-sensitized solar cells, Journal of Power Sources, 264 (2014) 15-21.
[52] E.N. Kumar, R. Jose, P.S. Archana, C. Vijila, M.M. Yusoff, S. Ramakrishna, High performance dye-sensitized solar cells with record open circuit voltage using tin oxide nanoflowers developed by electrospinning, Energy & Environmental Science, 5 (2012) 5401-5407.
[53] T. Krishnamoorthy, M.Z. Tang, A. Verma, A.S. Nair, D. Pliszka, S.G. Mhaisalkar, S. Ramakrishna, A facile route to vertically aligned electrospun SnO2 nanowires on a transparent conducting oxide substrate for dye-sensitized solar cells, Journal of Materials Chemistry, 22 (2012) 2166-2172.
[54] J.T. Park, C.S. Lee, J.H. Kim, One-pot synthesis of hierarchical mesoporous SnO2 spheres using a graft copolymer: enhanced photovoltaic and photocatalytic performance, RSC Advances, 4 (2014) 31452-31461.

## Figures and Figure captions

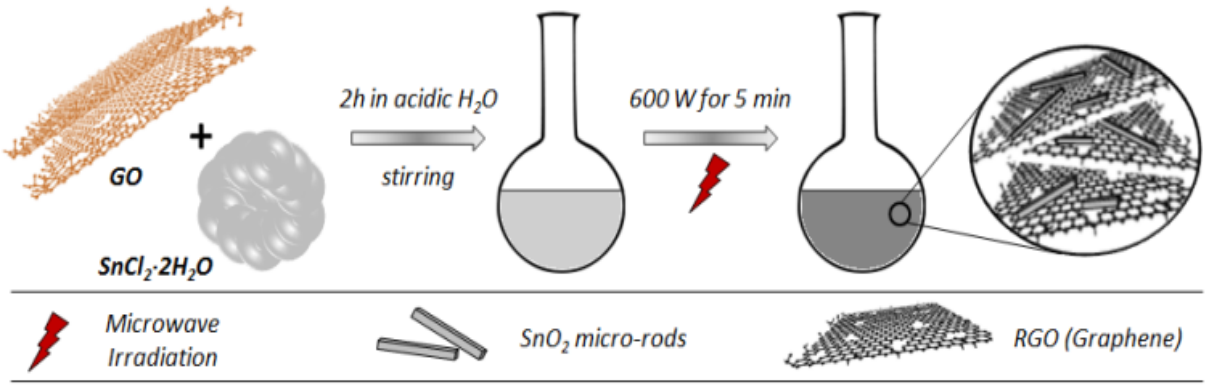


**Scheme. 1.** Synthetic procedure of $SnO_2$–RGO hybrid structure.

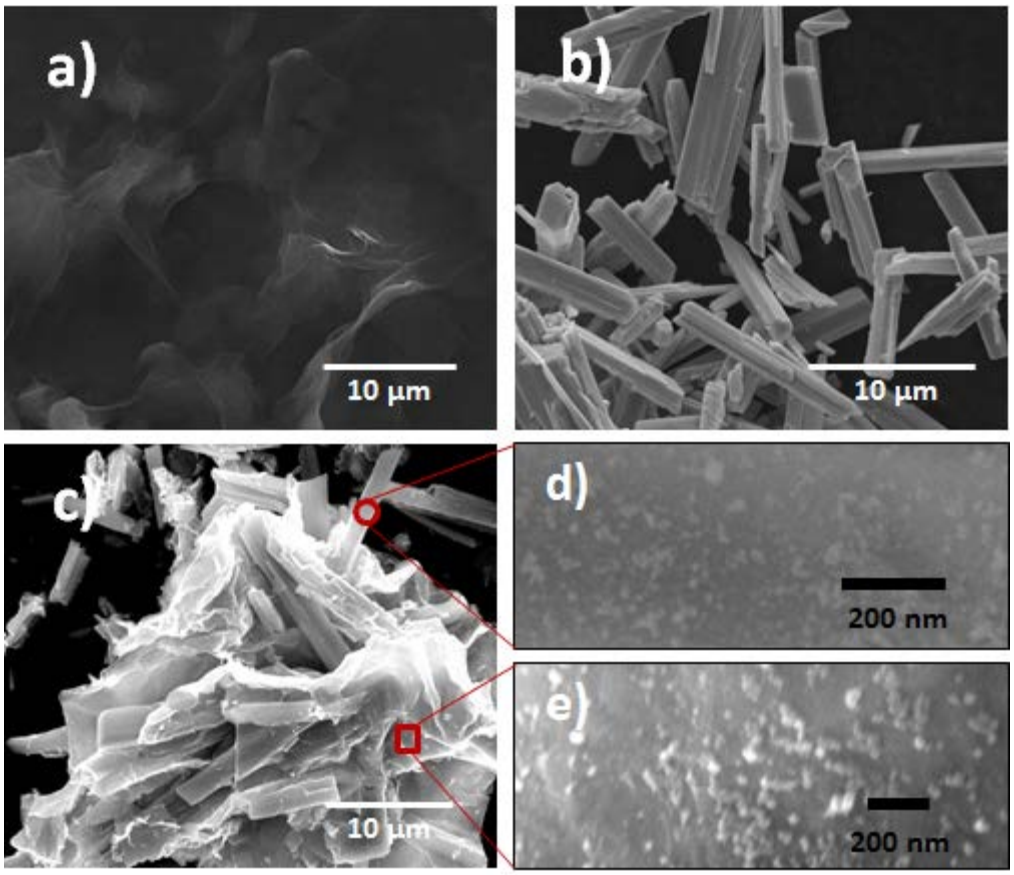


**Fig. 1.** SEM images of (a) GO, (b) $SnO_2$ micro-rod and (c) $SnO_2$-RGO hybrid. High resolution SEM images of (d) $SnO_2$ micro-rod and (e) RGO sheet in the hybrid showing that small $SnO_2$ nanoparticles are formed on $SnO_2$ and RGO surface.

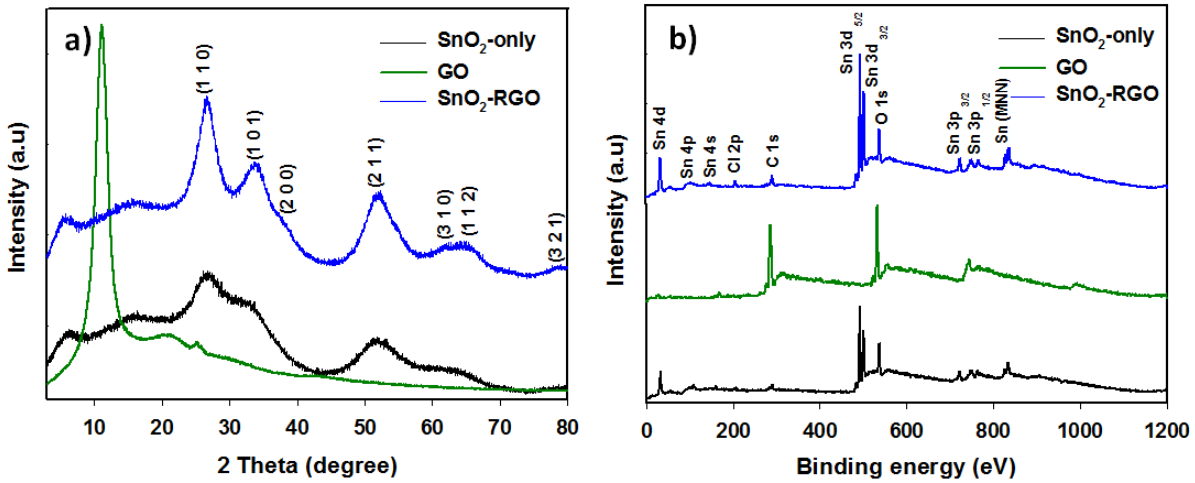


**Fig. 2.** (a) XRD patterns and (b) XPS survey spectra of the samples.

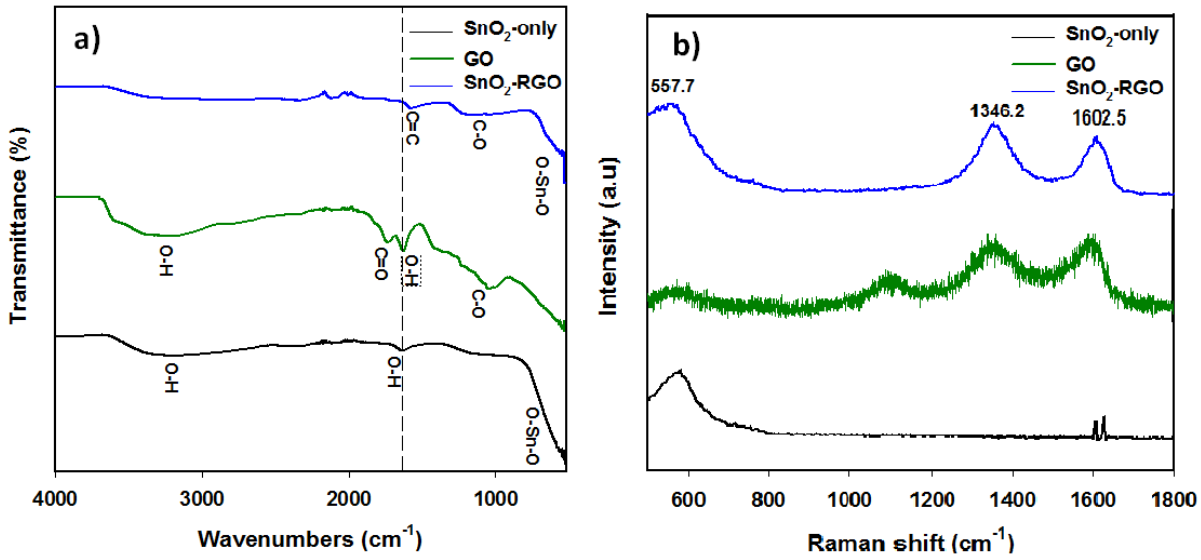


**Fig. 3.** (a) ATR-FTIR and (b) Raman spectra of $SnO_2$-only, GO and $SnO_2$-RGO hybrid materials. Long dash line in ATR-FTIR spectra proves that "–OH" is different from the "C=C" in the hybrid.

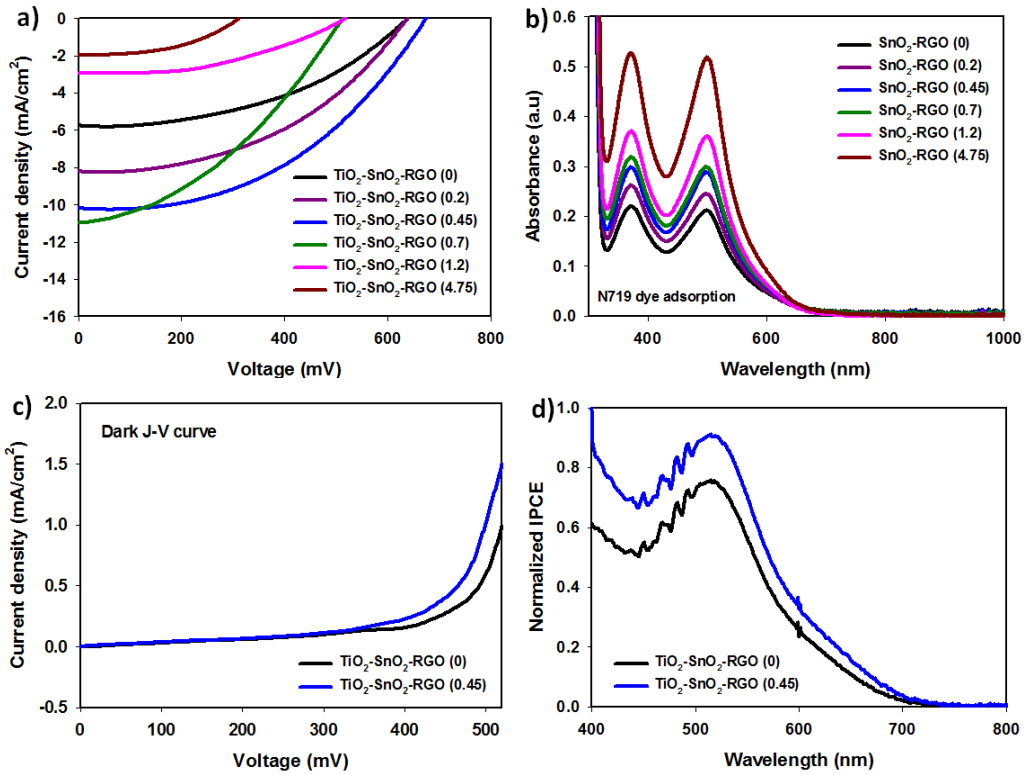


**Fig. 4.** (a) *J–V* curves of DSSCs assembled with different RGO content in the $TiO_2$-$SnO_2$ photoanode measured under AM 1.5G illumination at 100 mW $cm^{-2}$. (b) UV-vis spectra of N719 dye molecules desorbed from $SnO_2$ films with different amount of RGO using 0.1 M NaOH solution. (c) *J–V* curves of DSSCs fabricated without and with RGO in the $SnO_2$ photoanodes measured under the dark state. (d) Normalized IPCE value of DSSCs fabricated based on $TiO_2$-$SnO_2$ photoanodes with (0.45 wt%) and without RGO.

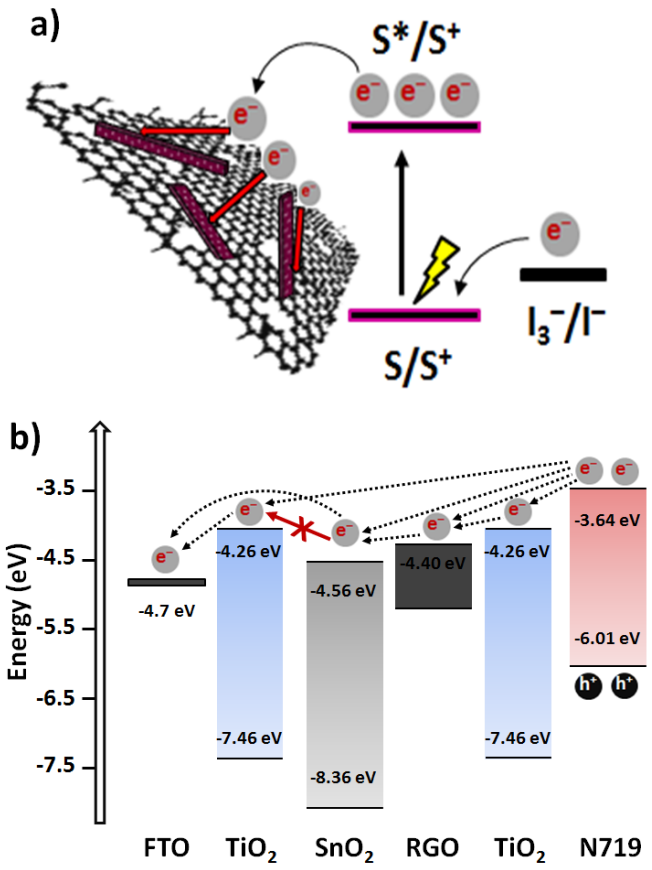


**Fig. 5.** (a) A possible mechanism for the enhanced electron transfer in $SnO_2$-RGO hybrid. (b) Energy level diagram for the $TiCl_4$ treated $SnO_2$ photoanode with RGO.

**Table 1.** PV parameters of the DSSCs fabricated based on $SnO_2$ photoanodes with different RGO content. Average values and the standard deviations of the DSSCs are shown based on at least three cells for each device. Parameters of the best cells are highlighted in **bold**.

| Device | RGO, wt% | $J_{sc}$, (mA $cm^{-2}$) | $V_{oc}$, (V) | FF | $\eta$ (%) |
|---|---|---|---|---|---|
| $TiO_2$-$SnO_2$-RGO (0) | 0 | **5.735**; 4.78 ± 0.95 | **0.64**; 0.64 ± 0.01 | **0.45**; 0.43 ± 0.04 | **1.65**; 1.28 ± 0.52 |
| $TiO_2$-$SnO_2$-RGO (0.2) | 0.2 | **8.196**; 8.20 ± 0.15 | **0.64**; 0.63 ± 0.01 | **0.45**; 0.44 ± 0.01 | **2.36**; 2.27 ± 0.07 |
| $TiO_2$-$SnO_2$-RGO (0.45) | 0.45 | **10.185**; 9.41 ± 1.00 | **0.67**; 0.67 ± 0.01 | **0.46**; 0.46 ± 0.01 | **3.16**; 2.94 ± 0.24 |
| $TiO_2$-$SnO_2$-RGO (0.7) | 0.7 | **10.954**; 10.23 ± 0.88 | **0.52**; 0.50 ± 0.02 | **0.39**; 0.41 ± 0.04 | **2.15**; 2.08 ± 0.17 |
| $TiO_2$-$SnO_2$-RGO (1.2) | 1.2 | **2.914**; 2.91 ± 0.03 | **0.52**; 0.51 ± 0.01 | **0.45**; 0.44 ± 0.01 | **0.68**; 0.66 ± 0.03 |
| $TiO_2$-$SnO_2$-RGO (4.75) | 4.75 | **1.984**; 1.74 ± 0.26 | **0.31**; 0.27 ± 0.05 | **0.46**; 0.43 ± 0.04 | **0.29**; 0.22 ± 0.08 |

**Table 2.** PV parameters of the DSSCs fabricated based on various $SnO_2$ photoanode structures and our best performing cell ($TiO_2$-$SnO_2$-RGO (0.45).

| Structure | Ref. | $J_{sc}$, (mA $cm^{-2}$) | $V_{oc}$, (V) | FF | $\eta$ (%) |
|---|---|---|---|---|---|
| This study | - | 10.18 | 0.67 | 0.46 | 3.16 |
| $SnO_2$ nanoparticles | [49] | 7.63 | 0.35 | 0.43 | 1.14 |
| $SnO_2$ nanoparticles | [44] | 4.90 | 0.40 | 0.51 | 1.00 |
| $SnO_2$ nanoparticles | [50] | 7.90 | 0.47 | 0.55 | 2.03 |
| $SnO_2$ nanofibers | [51] | 7.04 | 0.51 | 0.38 | 1.34 |
| $SnO_2$ multiporous NFs | [12] | 10.0 | 0.44 | 0.45 | 2.00 |
| $SnO_2$ nanoflowers | [52] | 7.30 | 0.70 | 0.60 | 3.00 |
| $SnO_2$ NWs + NPs | [53] | 9.90 | 0.53 | 0.49 | 2.53 |
| $SnO_2$ spheres (hierarchical mesoporous) | [54] | 12.3 | 0.52 | 0.58 | 3.70 |

## Supplementary Information

# Incorporation of Graphene into $SnO_2$ Photoanode for Dye-Sensitized Solar Cells

Munkhbayar Batmunkh,[a,b,1] Mahnaz Dadkhah,[b,1] Cameron J. Shearer,[b] Mark J. Biggs,[a,c] and Joseph G. Shapter [b,*]

[a] *School of Chemical Engineering, The University of Adelaide, Adelaide, South Australia 5005, Australia*

[b] *School of Chemical and Physical Sciences, Flinders University, Bedford Park, Adelaide, South Australia 5001, Australia*

[c] *School of Science, Loughborough University, Loughborough, Leicestershire, LE11 3TU, UK*

[1] These authors contributed equally

Corresponding Author:
*joe.shapter@flinders.edu.au

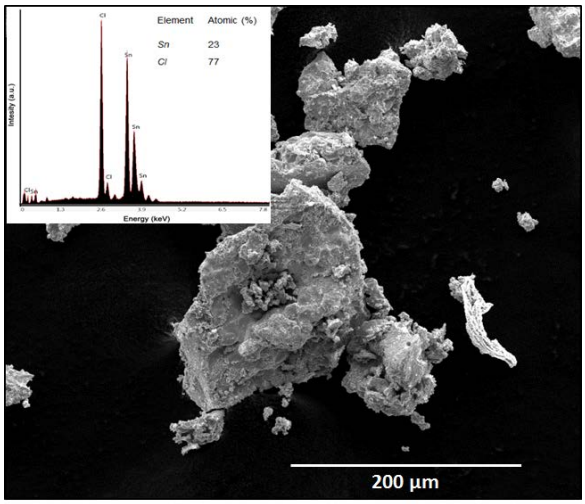


**Fig. S1.** SEM image and EDX elemental analysis (inset) of $SnCl_2 \cdot 2H_2O$ sample (used as the starting material).

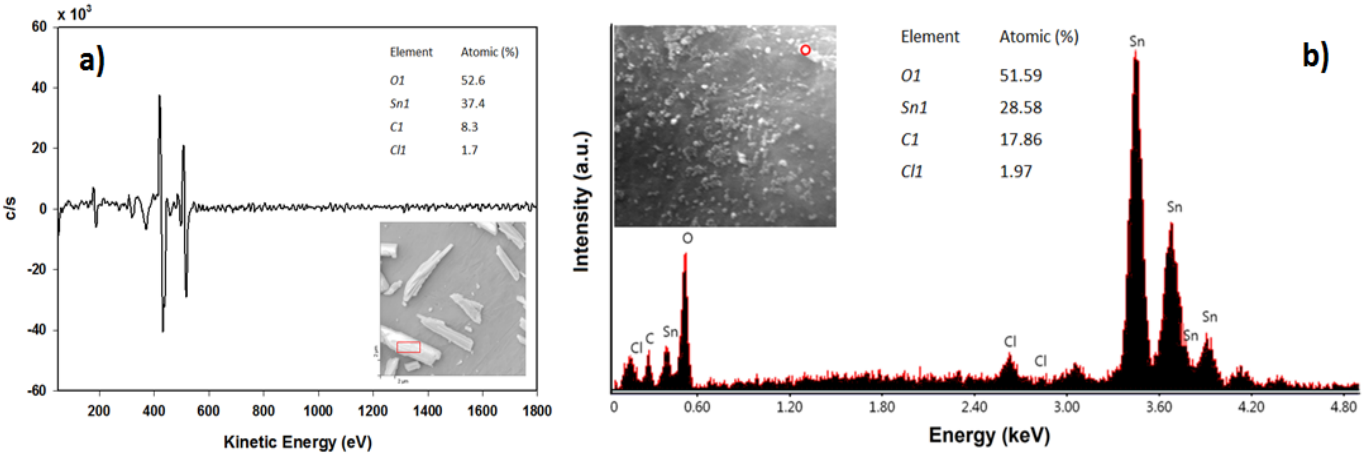


**Fig. S2.** (a) Auger and (b) EDX elemental analysis on the selected area (highlighted by red rectangle in (a) and circle in (b)) of the corresponding SEM images of $SnO_2$-RGO hybrid, as shown in the inset in b).

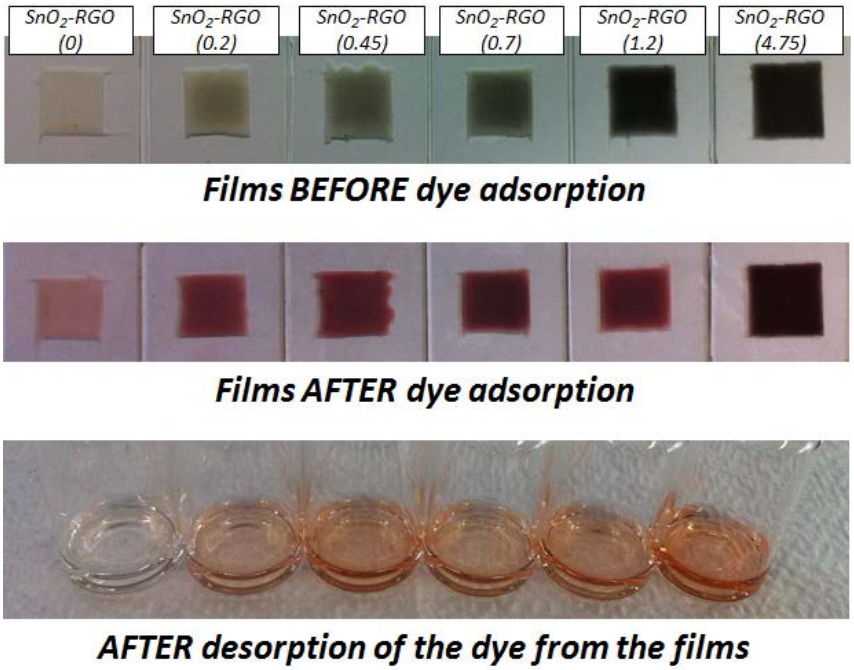


**Fig. S3.** Dye adsorption capability of the films ($SnO_2$-RGO (X)) with different RGO content. In $SnO_2$-RGO (X), the value of X indicates the weight concentration (wt%) of RGO in the hybrid. For instance, the concentration of RGO in the $SnO_2$-RGO (0.45) was 0.45 wt%.

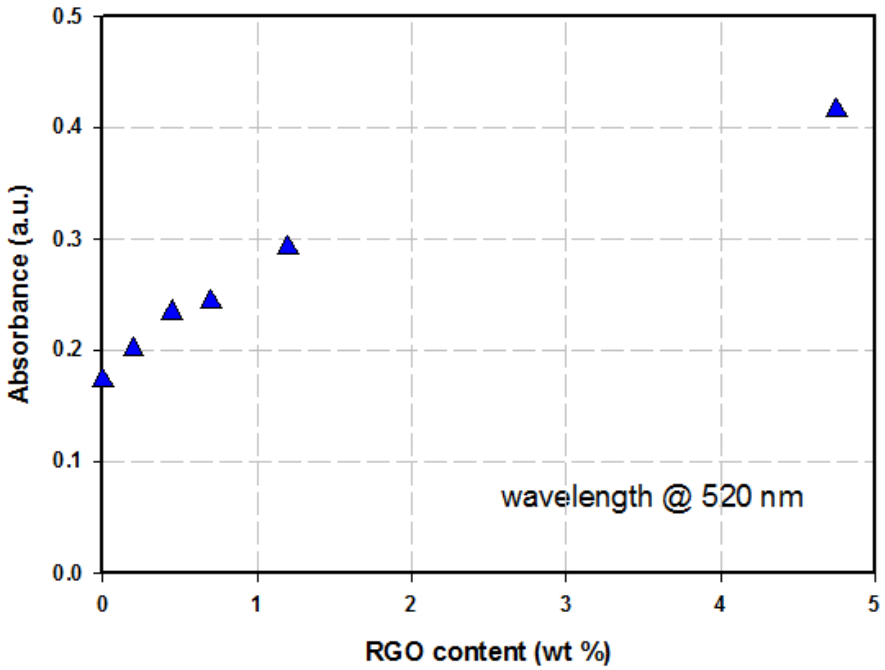


**Fig. S4.** The absorbance of these solutions at a wavelength of 520 nm.

Fig. S5a shows the J–V curves of DSSCs assembled with different RGO in the $SnO_2$ photoanodes (without any $TiCl_4$ treatment on the photoanode).The overall trend in the efficiency changes (increased after adding appropriate amount of RGO into the $SnO_2$ and decreased at too high concentration of RGO in the photoanodes) of DSSCs without and with $TiCl_4$ treatment was very similar, demonstrating that adding RGO into $SnO_2$ photoanode can enhance the PV efficiency, regardless of additional $TiCl_4$ treatment. A possible energy diagram for $SnO_2$-RGO photoanode based DSSC is shown in Fig. S5b. In this device structure, RGO enhances the electron transport rate and can also act as a bridge between dye and $SnO_2$. Notably, the efficiency of our $SnO_2$-only based DSSC was within the range (ranging from 0.6% to 1.0%) of previously reported values [1-3].

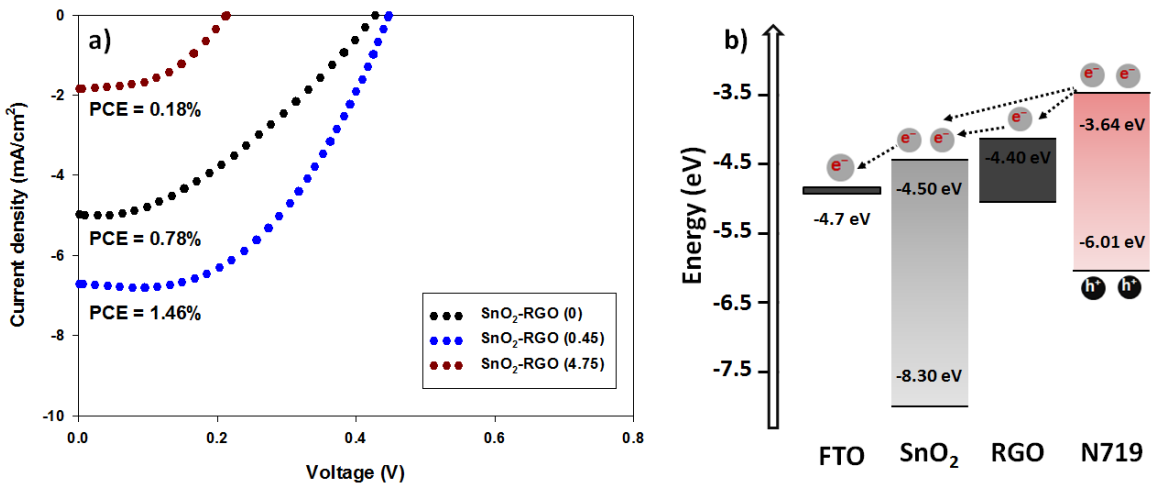


**Fig. S5.** (a) J–V curves of DSSCs fabricated with different RGO content in the $SnO_2$ photoanode without the $TiO_2$ blocking layer and (b) an energy level diagram for the $SnO_2$-RGO photoanode without any $TiO_2$ blocking layer.

It should be noted that $TiO_2$ was formed on the FTO by $TiCl_4$ treatment. However, it is well established that the $TiO_2$ does not completely cover FTO which makes electron transfer process possible between $SnO_2$ and FTO [4–7]. In order to prove that the coverage of $TiO_2$ during from $TiCl_4$ treatment on FTO is not 100%, DSSCs with a structure FTO/$TiO_2$/$SnO_2$/dye/electrolyte/Pt/FTO (without the second $TiCl_4$ treatment) were fabricated and their J-V characteristics are illustrated in Fig. S6a. It is reasonable to

expect that the DSSC fabricated with such structure cannot work if the $TiO_2$ completely (100%) covered the FTO because the conduction band of $TiO_2$ (-4.25 eV) is higher than that of $SnO_2$ (-4.56 eV) and thus energy transfer from the $SnO_2$ to the FTO through $TiO_2$ layer would not be feasible (see Fig. S6b). Interestingly, the fabricated DSSC exhibited a good efficiency (1.17%) with increased $V_{oc}$ value, as compared to $SnO_2$ photoanode based DSSC without any blocking layer $TiCl_4$ treatment. Cells with the $TiO_2$ blocking layer only and $SnO_2$–free photoanode give a very poor performance (see Fig. S7). The improvement in efficiency for the cell of Fig. S6 compared to the cell without graphene of Fig. S5 means that while the $TiO_2$ on the FTO must play a small role in the cell, the $SnO_2$ must also be in direct contact with the FTO and able to transfer electrons. This clearly show the thin $TiO_2$ layer does not cover the FTO completely and electron transfer from both oxides must occur. The incomplete coverage and thinness of $TiO_2$ on the FTO means the majority of the photovoltaic performance is from the $SnO_2$ layer.

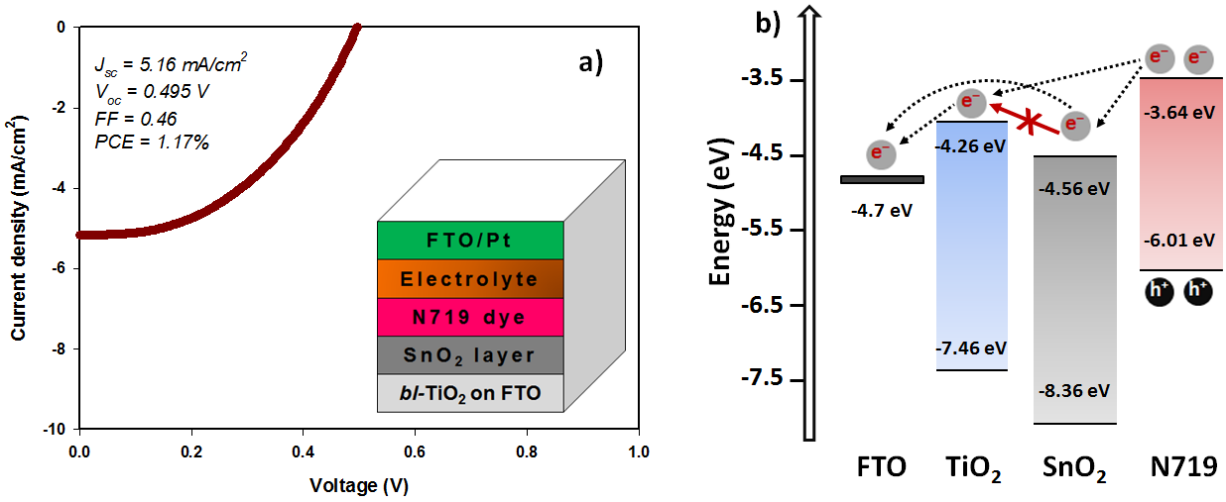


**Fig. S6.** (a) J–V curves of DSSC device assembled with the photoanode structure of FTO/thin $TiO_2$/$SnO_2$/dye (without second $TiCl_4$ treatment). Inset shows the device structure. (b) A possible energy level diagram for this DSSC photoanode.

In addition, only $TiCl_4$ treated FTO as a photoanode based DSSC was fabricated and its performance is depicted in Fig. S7. For this experiment, the cleaned FTO was immersed in a 40 mM $TiCl_4$ aqueous

solution at 70°C for 30 min, followed by drying with $N_2$ gas and annealing at 450°C for 30 min. After cooling to room temperature, second $TiCl_4$ treatment was performed in a same manner. Finally the film was sintered at 450°C for 30 min and then exposed the dye solution as before. As a result, the fabricated cell showed high $V_{oc}$ value, but its PCE was very poor (0.13%). This result is reasonable since the $V_{oc}$ parameter is determined by the energy level difference between the conduction band of semiconducting photoanode material ($TiO_2$ here in this device) and the potential energy of the electrolyte. The very low $J_{sc}$ value of this cell is due to the insufficient dye-loading into the photoanode film as only very thin $TiO_2$ and low surface area layer is formed on the FTO. A poor fill factor value could also be associated with the incomplete coverage of $TiO_2$ on the FTO. These results again show that the $SnO_2$ is the main active element of the these photoanodes.

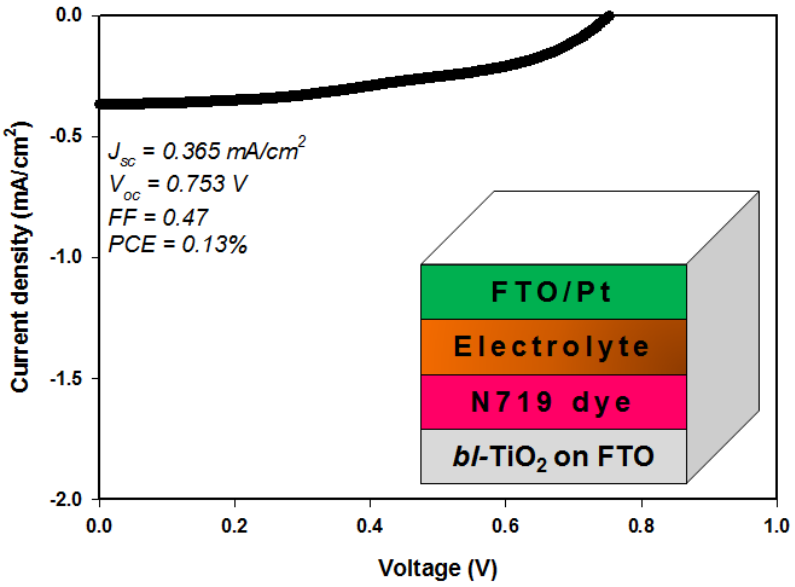


**Fig. S7.** J–V curves of DSSC fabricated with thin $TiO_2$ layers on FTO as a photoanode. Notably, $TiO_2$ layers were formed on the FTO by 2 times $TiCl_4$ treatment as was done for the normal device structure. Inset shows the device structure.

**Table S1**. Electrical parameters of $SnO_2$ photoanode without and with RGO and their DSSCs.

| Sample | Sheet resistance, $R_s$ (Ω/□) | Series resistance, $R_{series}$ (Ω) | Shunt resistance, $R_{shunt}$ (Ω) |
|---|---|---|---|
| $TiO_2$-$SnO_2$-RGO (0) | 4.51 x $10^6$ | 167.0 | 1600 |
| $TiO_2$-$SnO_2$-RGO (0.45) | 1.81 x $10^6$ | 97.9 | 1920 |

**Reference**


[1] E. Ramasamy, J. Lee, Ordered mesoporous $SnO_2$−based photoanodes for high-performance dye-sensitized solar cells, J. Phys. Chem. C, 114 (2010) 22032–22037.

[2] F. Gu, W. Huang, S. Wang, X. Cheng, Y. Hu, G. Li, Improved photoelectric conversion efficiency from titanium oxide-coupled tin oxide nanoparticles formed in flame, J Power Sources, 268 (2014) 922-927.

[3] E. N. Kumar, R. Jose, P. S. Archana, C. Vijila, M. M. Yusoff, S. Ramakrishna, High performance dye-sensitized solar cells with record open circuit voltage using tin oxide nanoflowers developed by electrospinning, Energy Environ. Sci, 5 (2012) 5401-5407.

[4] Z. Du, H. Zhang, H. Bao, X. Zhong, Optimization of $TiO_2$ photoanode films for highly efficient quantum dot-sensitized solar cells, Journal of Materials Chemistry A., 2 (2014) 13033-13040.

[5] S. Yang, Y. Hou, B. Zhang, X. H. Yang, W. Q. Fang, H. J. Zhao, H. G. Yang, Highly efficient overlayer derived from peroxotitanium for dye-sensitized solar cells, Journal of Materials Chemistry A., 1 (2013) 1374-1379.

[6] S.-K. Kim, M.-K. Son, S. Park, M.-S. Jeong, D. Savariraj, K. Prabakar, H.-J. Kim, The effect of $TiO_2$ compact layer in ZnO nanorod based CdS/CdSe quantum-dot sensitized solar cell, physica status solidi (a). 211 (2014) 1839-1843.

[7] H. Choi, C. Nahm, J. Kim, J. Moon, S. Nam, D.-R. Jung, B. Park, The effect of $TiCl_4$-treated $TiO_2$ compact layer on the performance of dye-sensitized solar cell, Current Applied Physics. 12 (2012) 737-741.